

Flat-Band Engineering with \mathcal{PT} Metamaterials: Compact Localized Flat-Band States

N. Lazarides^{1,2}, G. P. Tsironis^{1,2}

¹Physics Department, University of Crete, P. O. Box 2208, 71003 Heraklion, Greece

²National University of Science and Technology "MISiS", Leninsky Prospekt 4, Moscow, 119049, Russia

(Dated: October 8, 2018)

The conditions leading to flat (dispersionless) frequency bands in truly one-dimensional parity-time (\mathcal{PT}) symmetric metamaterials comprising split-ring resonators arranged in a binary pattern are obtained analytically. In this paradigmatic system, flat-bands may arise from tailoring the model parameters, and not from geometrical effects. For parameter values tailored to flatten one of the bands in the spectrum, the solution of the quadratic eigenvalue problem reveals the existence of compact, two-site localized eigenmodes. Numerical simulations confirm the existence and the dynamic stability of such modes, which are formed through the evolution of single-site initial excitations without disorder or nonlinearity.

PACS numbers: 03.65.Ge, 63.20.D-, 63.20.Pw, 78.67.Pt

Considerable research effort has focused the last decades in the investigation and development of artificial structures such as *metamaterials* [1, 2] and *parity-time (\mathcal{PT} -) symmetric materials* [3], which exhibit properties not available in natural materials. Inspired by Veselago's ideas [4], Pendry and his collaborators suggested using split-ring resonator (SRR) arrays [5] and thin-wire arrays [6] to achieve effectively negative permeability and permittivity, respectively, in overlapping frequency bands. The combination of these two subsystems into a single artificial structure results in a negative refractive index medium, whose first realization was made in the turn of the 21st century [7]. The \mathcal{PT} -symmetric materials originated from the ideas and notions of non-Hermitian Quantum Mechanics [8, 9], which were later transferred to optical lattices [10, 11] and electronic systems [12]. The application of these ideas in electronic circuits has provided easily accessible experimental configurations as well as a link to the electrical circuit picture of SRR-based metamaterials; the latter may acquire \mathcal{PT} -symmetry which relies on balanced gain and loss [13]. Such \mathcal{PT} metamaterials (PTMMs) may serve as paradigmatic systems that exhibit isolated flat (dispersionless) bands.

Flat bands (FBs) have been first in the electronic band structure of semiconductor heterostructures [14] and superconducting cuprates [15]. Recently, the possibility for dispersionless (diffraction-free in optics) propagation and robust localization in FB systems has initiated intensive research on simple crystal structures such as Lieb lattices [16–20] as well as Kagomé, cross-stich, and diamond lattices that allow for precise FB engineering, even in the presence of disorder and/or nonlinearity [21, 22] (see Ref. [23] for a recent review). Furthermore, almost FBs have been obtained in complex networks [24]. Note that in Ref. [18, 19], \mathcal{PT} -symmetry is introduced as a perturbation in lattices which possess FBs. Research on more complex systems such as Weyl semimetal superconductors [25], organometallic frameworks [26], honeycomb optical lattices [27], and graphene [28], has revealed the

existence of FBs in those systems as well. Moreover, topological FBs have been identified in various systems [29–31], and fractional quantum Hall states at zero magnetic field were found in systems with *nearly* FBs [32–34]. FBs are typically associated with the appearance of compact localized modes in certain lattices without any nonlinearity and/or disorder. Recently, the first experimental observation of diffraction-free propagation of such FB modes in Lieb photonic lattices has been reported [35, 36].

Here, a truly one-dimensional (1D) PTMM paradigmatic model in which an isolated FB arises from tailoring its parameters and not from geometrical effects, is presented. A condition for the existence of a FB is obtained analytically; compact, two-site localized eigenmodes are found by solving the corresponding quadratic eigenvalue problem (QEP) whenever that condition is satisfied. The existence and dynamic stability of these modes is confirmed by numerical simulations.

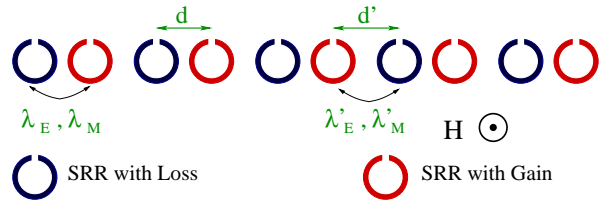


FIG. 1: (Color online) Schematic of a \mathcal{PT} metamaterial comprising split-ring resonators arranged in a 1D binary pattern.

Consider a 1D array of SRRs arranged in a binary pattern (Fig. 1); within each dimer, the SRR at right has gain while the one at left has equal amount of loss. The SRRs interact both electrically and magnetically through dipole-dipole forces [37, 38] and can be regarded as RLC circuits, featuring a resistance R , an inductance L , and a capacitance C . Gain can be provided to an SRR by, e.g., mounting to its slit a negative resistance electronic device such as an Esaki diode [39]. Using equivalent cir-

cuit models, the equations governing the dynamics of the charge q_n stored in the capacitor of the n th SRR are obtained as [13, 40]

$$\lambda'_M \ddot{q}_{2n} + \ddot{q}_{2n+1} + \lambda_M \ddot{q}_{2n+2} + \gamma \dot{q}_{2n+1} + q_{2n+1} = -\{\lambda'_E q_{2n} + \lambda_E q_{2n+2}\}, \quad (1)$$

$$\lambda_M \ddot{q}_{2n-1} + \ddot{q}_{2n} + \lambda'_M \ddot{q}_{2n+1} - \gamma \dot{q}_{2n} + q_{2n} = -\{\lambda_E q_{2n-1} + \lambda'_E q_{2n+1}\}, \quad (2)$$

where λ_E and λ_M (λ'_E and λ'_M) are respectively the electric and magnetic coupling coefficients between SRRs with center-to-center distance d (d'), γ is the gain/loss coefficient ($\gamma > 0$), and the overdots denote derivation with respect to the normalized temporal variable $\tau = \omega_{LC} t$, with $\omega_{LC}^{-1} = \sqrt{LC}$.

By substituting $q_{2n} = A \exp[i(2n\kappa - \Omega\tau)]$ and $q_{2n+1} = B \exp[i((2n+1)\kappa - \Omega\tau)]$ into Eqs. (1) and (2), where κ is the normalized wavevector and Ω is the frequency in units of ω_{LC} , and requesting nontrivial solutions for the resulting stationary problem, we obtain

$$\Omega_\kappa^2 = \frac{1}{2a} \left(-b \pm \sqrt{b^2 - 4ac} \right), \quad (3)$$

where $a = 1 - (\lambda_M^2 + \lambda'_M{}^2) - 2\lambda_M \lambda'_M \cos(2\kappa)$, $b = 2(\lambda_E \lambda_M + \lambda'_E \lambda'_M) + 2(\lambda_E \lambda'_M + \lambda'_E \lambda_M) \cos(2\kappa) - 2 + \gamma^2$, and $c = 1 - (\lambda_E^2 + \lambda'_E{}^2) - 2\lambda_E \lambda'_E \cos(2\kappa)$. In the exact \mathcal{PT} phase, Eq. (3) gives a gapped spectrum with two frequency bands separated by a gap.

The FB condition is obtained by requesting $d(\Omega_\kappa^2)/d\kappa = 0$ for any κ in the first Brillouin zone. After tedious calculations, we get

$$\left[(1 - \lambda_M^2) / \mathcal{R}' + \mathcal{G} + \mathcal{R}' (1 - \lambda_E^2) \right] \times \left[(1 - \lambda'_M{}^2) / \mathcal{R} + \mathcal{G}' + \mathcal{R} (1 - \lambda'_E{}^2) \right] = 0, \quad (4)$$

where $\mathcal{R} = \lambda_M / \lambda_E$, $\mathcal{R}' = \lambda'_M / \lambda'_E$, $\mathcal{G} = -2 + \gamma^2 + 2\lambda_E \lambda_M$, and $\mathcal{G}' = -2 + \gamma^2 + 2\lambda'_E \lambda'_M$. The values of \mathcal{R}' , λ_E , λ_M , and γ , for which the expression in the first squared brackets in Eq. (4) equals to zero, provide a physically acceptable parameter set which flattens the upper band of the spectrum over the whole Brillouin zone.

For such a parameter set, the calculated frequency spectrum (from Eq. (3)) contains a *completely flat, isolated upper band* (Fig. 2(a)) with zero group velocity v_g for any κ in the first Brillouin zone (inset). For the configuration of Fig. 1, the coupling coefficients between SRRs have been calculated (figure 1(a) in Ref. [38]). According to these data, the coupling coefficients used in Fig. 2(a) correspond to distances $d \sim 2$ and $d' \sim 3.7$ in units of the SRRs' radii, that seems in principle feasible. On the contrary, for parameter sets not satisfying Eq. (4), non-flat bands with κ -dependent group velocities v_g such as those shown in Fig. 2(b) are typically obtained. The band-boundaries (BBs), i.e., the extremal frequencies in each band, are shown as a function of γ in Fig. 2(c). For $\gamma < \gamma_c$ (unbroken \mathcal{PT} phase), the BBs of the upper band

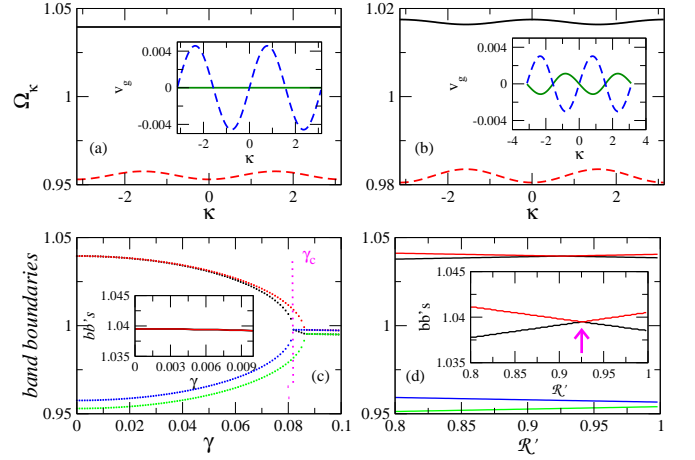


FIG. 2: (Color online) (a) Frequency bands $\Omega_\kappa(\kappa)$ for a \mathcal{PT} metamaterial with $\gamma = 0.003$, $\lambda_E = -0.123952$, $\lambda_M = -0.040128$, $\lambda'_E = -0.027$, and $\mathcal{R}' = 0.92547$. The upper band at $\Omega_\kappa \sim 1.03949$ (black-solid curve) is flat. Inset: The corresponding group velocities v_g ($= 0$ for the flat band). (b) Same as in (a) for $\gamma = 0.003$, $\lambda_E = -0.055$, $\lambda_M = -0.02$, $\lambda'_E = -0.027$, and $\mathcal{R}' = 0.92547$. (c) The band-boundaries as a function of γ for the coupling coefficients in (a). The vertical segment indicates $\gamma = \gamma_c$. Inset: Enlargement of the upper band-boundaries for low γ . (d) The band-boundaries as a function of \mathcal{R}' , with γ , λ_E , λ'_E , and λ_M as in (a). Inset: Enlargement of the boundaries of the upper band around the value of \mathcal{R}' for which the band is flat (shown in (a)).

(red and black dotted curves) practically coincide for a substantial interval of γ indicating zero bandwidth (i.e., a FB), while the width of the lower band (limited by the blue and green dotted curves) remains almost constant up to $\gamma = \gamma_c$. The flatness of the upper band for low γ can be seen more clearly in the inset. In Fig. 2(d), the BBs are plotted as a function of \mathcal{R}' ; the width of the upper band (limited by the red and black solid curves) consecutively decreases, goes through zero at a critical value of \mathcal{R}' indicated by the arrow, and increases with increasing \mathcal{R}' (see also inset). At that critical value of \mathcal{R}' the two bands coincide with those shown in Fig. 2(a).

Eqs. (1) and (2) can be written in matrix form as

$$\hat{\mathbf{M}}\ddot{\mathbf{Q}} = \hat{\mathbf{C}}_1\dot{\mathbf{Q}} + \hat{\mathbf{K}}\mathbf{Q}, \quad (5)$$

where $\mathbf{Q} = [q_1 \ q_2 \ \dots \ q_N]^T$ is an N -dimensional vector, with N being the total number of SRRs, and $\hat{\mathbf{M}}$, $\hat{\mathbf{K}}$, and $\hat{\mathbf{C}}_1$ are $N \times N$ matrices. The non-zero elements of the first two are $(\hat{\mathbf{K}})_{n,n} = -1$, $(\hat{\mathbf{M}})_{n,n} = +1$, for $n = 1, \dots, N$, $(\hat{\mathbf{K}})_{2m-1,2m} = (\hat{\mathbf{K}})_{2m,2m-1} = -\lambda_E$, $(\hat{\mathbf{M}})_{2m-1,2m} = (\hat{\mathbf{M}})_{2m,2m-1} = \lambda_M$, for $m = 1, \dots, N/2$, and $(\hat{\mathbf{K}})_{2m+1,2m} = (\hat{\mathbf{K}})_{2m,2m+1} = -\lambda'_E$, $(\hat{\mathbf{M}})_{2m+1,2m} = (\hat{\mathbf{M}})_{2m,2m+1} = \lambda'_M$, for $m = 1, \dots, N/2 - 1$. The matrix $\hat{\mathbf{C}}_1$ is diagonal, with $(\hat{\mathbf{C}}_1)_{n,n} = \gamma(-1)^n$ ($n = 1, \dots, N$). By substituting $\mathbf{Q} = \mathbf{Q}^e e^{i\Omega\tau}$ into Eqs. (5) we get

$$\left\{ \Omega^2 \hat{\mathbf{M}} + \Omega \hat{\mathbf{C}}_1 + \hat{\mathbf{K}} \right\} \mathbf{Q}^e = \hat{\mathbf{0}}, \quad (6)$$

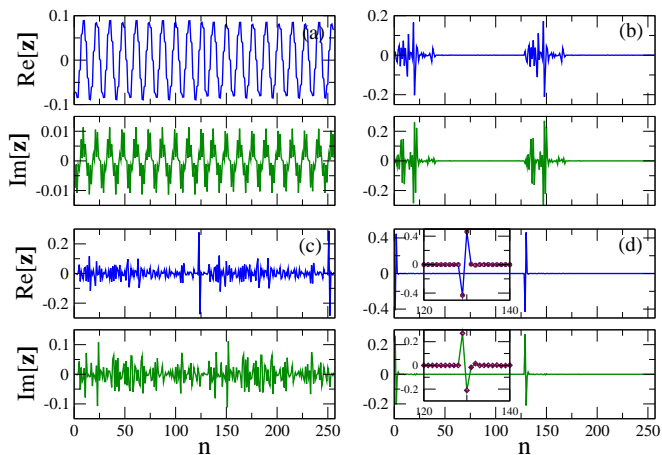


FIG. 3: (Color online) Real (blue) and imaginary (green) parts of the eigenmodes obtained by solving Eq. (7) for $N = 128$, $\gamma = 0.01$, $\lambda_E = -0.1200046$, $\lambda_M = -0.0400493$, $\lambda'_E = -0.027$, and $\mathcal{R}' = 0.9291948$. The eigenfrequency of the flat band is $\Omega_{FB} \simeq 1.03740$. (a) An extended eigenmode from the lower (non-flat) band. (b) A partially localized flat-band eigenmode. (c) A highly localized flat-band eigenmode. (d) The compact, two-site localized flat-band eigenmode. Insets: Enlargements around the localization region.

where $\hat{\mathbf{C}} \equiv i\hat{\mathbf{C}}_1$. Eq. (6) is a QEP [41] with Ω being the eigenvalue and \mathbf{Q}^e the corresponding N -dimensional eigenvector. It can be solved by standard eigenproblem solvers after its *linearization* by the classical augmentation procedure, which transforms square matrices of order N to $2N$ [42, 43] (see also Ref. [44]). Then, Eq. (6) is reduced to a standard eigenvalue problem (SEP)

$$\hat{\mathbf{D}}\mathbf{z} = \Omega\mathbf{z}, \quad \mathbf{z} = \begin{bmatrix} \mathbf{Q}^e \\ \Omega\mathbf{Q}^e \end{bmatrix}, \quad \hat{\mathbf{D}} = \begin{bmatrix} \hat{\mathbf{0}} & \hat{\mathbf{I}} \\ -\hat{\mathbf{M}}^{-1}\hat{\mathbf{K}} & -\hat{\mathbf{M}}^{-1}\hat{\mathbf{C}} \end{bmatrix}, \quad (7)$$

where I is the $N \times N$ identity matrix and $\hat{\mathbf{M}}^{-1}$ the inverse of $\hat{\mathbf{M}}$. In what follows, $\gamma < \gamma_c$ so that the system is in the exact (unbroken) \mathcal{PT} phase, and therefore all its eigenvalues are real. Some of its eigenmodes \mathbf{Q}^e are shown in Fig. 3. The eigenmodes from the non-flat (lower) band are extended, as in Fig. 3(a). The other three eigenmodes in Fig. 3 belong to the flat (upper) band, and therefore they correspond to the same eigenvalue Ω_{FB} . Figs. 3(b), (c), and (d) show a partially localized, a highly localized, and a compact two-site localized eigenmode, respectively. The insets in Fig. 3(d) enlarge the localization region. In the light of these findings, it would be expected that the PTMM in the exact phase supports compact localized excitations which in general could be expressed as linear superpositions of a small number of eigenmodes. The existence of compact localized eigenvectors in a class of FB models has been also demonstrated in Ref. [45].

Eqs. (1) and (2), implemented with free-end boundary conditions $q_0(\tau) = q_{N+1}(\tau) = 0$, are integrated in time

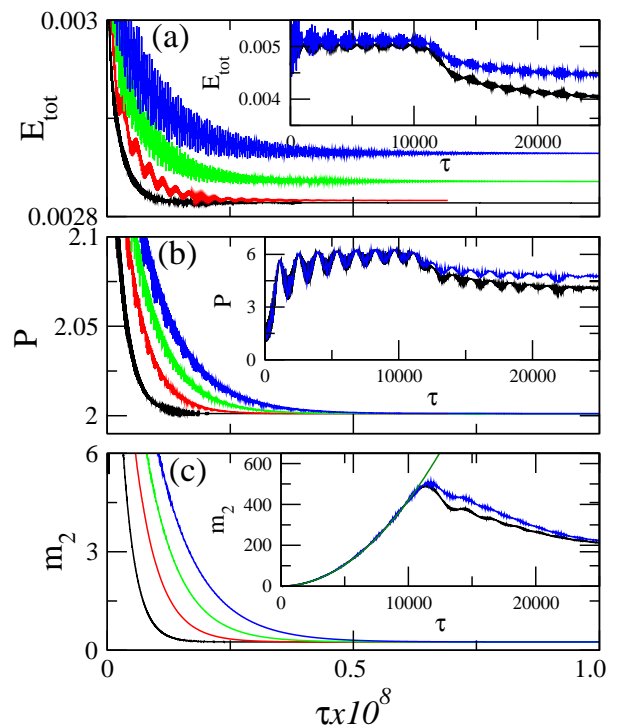


FIG. 4: (Color online) Total energy E_{tot} (a), energetic participation number P (b), and second moment m_2 (c), as functions of τ for $N = 128$, $N_e = 16$, and $\gamma = 0.003$, $\lambda_E = -0.123952$, $\lambda_M = -0.040128$, $\mathcal{R}' = 0.92547$ (black); $\gamma = 0.006$, $\lambda_E = -0.120021$, $\lambda_M = -0.0400518$, $\mathcal{R}' = 0.9288096$ (red); $\gamma = 0.009$, $\lambda_E = -0.1200284$, $\lambda_M = -0.0399891$, $\mathcal{R}' = 0.9290096$ (green); $\gamma = 0.012$, $\lambda_E = -0.120122$, $\lambda_M = -0.0400118$, $\mathcal{R}' = 0.9293204$ (blue). Insets: The curves for $\gamma = 0.003$ (black) and 0.012 (blue) in a short time-scale. In the inset in (c), the curve $4.2 \times 10^{-6}\tau^2$ (green) is also plotted.

with a standard 4th order Runge-Kutta algorithm. The initial conditions are single-site excitations of the form $q_{n=N/2+1}(\tau=0) = A$, $q_n(\tau=0) = 0$ for $n \neq N/2+1$, and $\dot{q}_n(\tau=0) = 0$ for any n (typically $A = 0.1$). For N_e SRRs at each end of the PTMM, gain has been replaced by equal amount of loss; these lossy parts remove the excessive energy provided by the initial condition towards the formation of a compact localized FB state. In Fig. 4, the total energy

$$E_{tot} = \frac{1}{2} \left\{ \dot{\mathbf{Q}}^T \dot{\mathbf{Q}} + \mathbf{Q}^T \mathbf{Q} + \mathbf{Q}^T \hat{\mathbf{K}} \mathbf{Q} + \dot{\mathbf{Q}}^T \hat{\mathbf{M}} \dot{\mathbf{Q}} \right\}, \quad (8)$$

the (energetic) participation number $P = 1/\sum_n \epsilon_n^2$, and the second moment $m_2 = \sum_n (n - \bar{n})^2 \epsilon_n$, where $\bar{n} = \sum_n n \epsilon_n$ is the center of energy with $\epsilon_n = E_n/E_{tot}$ being the energy density, are shown as functions of τ . The four curves are obtained for parameter sets which satisfy the FB condition; the coupling coefficients have very similar values, while γ increases from 0.03 to 0.12 in steps of 0.03. In all cases, a steady FB state is reached at the end of the integration time; however, the transient period is longer and E_{tot} is higher for higher γ . In the

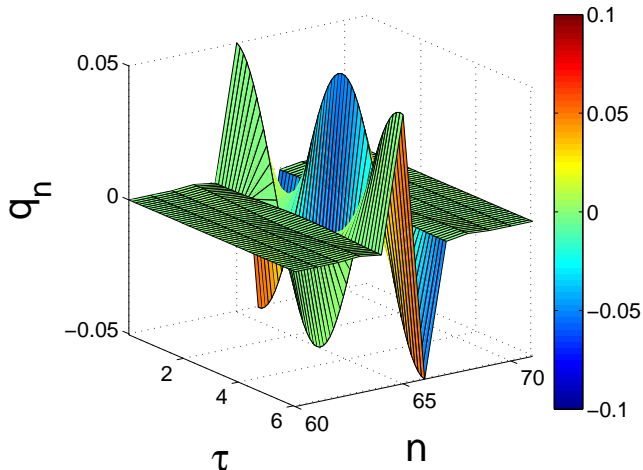


FIG. 5: (Color online) Spatiotemporal diagram of the charges q_n after $\sim 10^8$ time units of integration for $\gamma = 0.01$, $\lambda_E = -0.1200046$, $\lambda_M = -0.0400493$, $\mathcal{R}' = 0.9291948$, $N = 128$, $N_e = 16$ ($\Omega_{FB} \simeq 1.03740$). Only part of the \mathcal{PT} metamaterial is shown for clarity.

insets of Figs. 4(a), 4(b), and 4(c), the quantities E_{tot} , P , and m_2 , respectively, are plotted for the first 25,000 time units (t.u.). The energy E_{tot} strongly fluctuates, but it remains on average constant until $\tau \sim 12,000$ t.u. At the same time, P increases while fluctuating strongly and reaches $P = 6$, while m_2 increases $\propto \tau^2$ indicating ballistic spreading of the initial state. Around $\tau \sim 12,000$ t.u., the energy which spreads out from the initial state has reached the lossy ends of the PTMM where it is dissipated. After that time, E_{tot} , P , and m_2 decrease gradually until they saturate to constant values with vanishingly small fluctuations, indicating that a steady state has been reached. The constancy of m_2 , in particular, indicates that energy spreading has been stopped. Part of the initial excitation remains localized on two SRRs, as indicated by the value of $P = 2$ which measures the number of the energetically strongest excited sites [46].

Inspection of the $q_n(\tau)$ in Fig. 5 reveals that the excitation is localized to only two SRRs. The charges stored in the capacitors of these SRRs oscillate in anti-phase with frequency Ω_{FB} ; charge oscillations in the rest of the SRRs seems to have vanishingly small amplitude (see also Fig. 6(a)). Note that if the FB condition Eq. (4) is not satisfied, the initial excitations disperse rapidly in the lattice without leaving behind any trace of localization. Compact localized excitations often appear both in continuous [47] and discrete [48, 49] systems with nonlinear dispersion. In the latter, the tails of such excitations decay as a stretched exponential or superexponential [48]. Here, the compact localized states appear due to the FB without nonlinearity or disorder, and hence there are significant differences. In Fig. 6(b), the quantity $y_n = \ln \left[\frac{1}{2} (|q_{2n-1}| + |q_{2n}|) \right]$ is plotted as a function of n ;

the three curves correspond to different integration times, τ_0 . In obtaining the results in Fig. 6(b), convergence to a steady localized FB state was accelerated by continually eliminating the energy spreading away from the localization region during half of the integration time (see [44]). The almost horizontal segments between $16 \lesssim n \lesssim 63$ and $66 \lesssim n \lesssim 112$ (i.e., those parts of the lattice which do not belong either to the lossy ends nor to the localization region) correspond to the tails of the localized FB states. With increasing τ_0 , the tails become more and more negative until they saturate at $y_n \sim -35$ (the limit of double precision arithmetics) at $\tau_0 \sim 2 \times 10^6$. In the inset, the y_n profile at $\tau_0 = 3 \times 10^6$ t.u. (black curve) is fitted by $y_n = b + (\alpha_0 - b) \exp [c(n - x_0)^2]$ (red curve), where $x_0 = 65.5$ and $\alpha_0 = -2.9887$ are obtained by the numerical data. The fitting parameters are $b = -35.684$ and $c = -0.109955$.

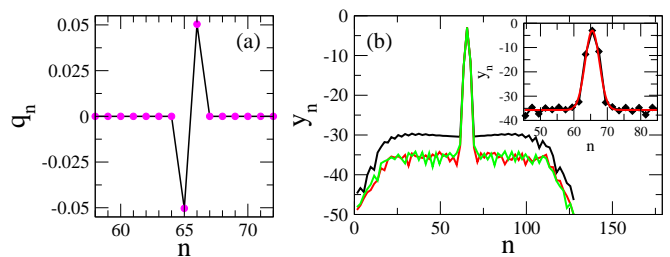


FIG. 6: (Color online) (a) Charge profile q_n at maximum oscillation amplitude. Parameters as in Fig. 5. (b) The function y_n after integration for $\tau_0 = 1.5 \times 10^6$ (black), 2×10^6 (red), 3×10^6 (green), time units. Inset: Fitting of y_n with an appropriate function (see text)

By tailoring the model parameters of a 1D PTMM comprising SRRs arranged in a binary pattern, isolated and completely FBs may appear. The analytical condition, which those parameters have to satisfy in order to flatten the upper band, is obtained. The solution of the QEP reveals the existence of compact, localized FB eigenmodes, in which most of the energy is concentrated in two SRRs. This is consistent with earlier results on nonlinear binary PTMMs, for which the fundamental discrete breathers are two-site ones (and not single-site ones) [13]. The formation of compact, two-site localized FB states from single-site initial excitations is numerically confirmed. Since the FB is isolated, these FB states could be continued into compact breather-like (nonlinear) excitations. Note that the possibility of flattening one of the bands of the spectrum is solely due to model parameter engineering, and not to any geometrical effects. In this aspect, the existence of two types of coupling between SRRs is crucial. Note also that similar results would have been obtained for $\gamma = 0$, in which case only three parameters, i.e., λ_E , λ_M , and \mathcal{R}' , should be matched. Notably, the band-flattening capability is not harmed by the \mathcal{PT} symmetry, as long as the PTMM is in the exact \mathcal{PT} phase.

Acknowledgements.- This work is partially supported by the Ministry of Education and Science of the Russian Federation in the framework of the Increase Competitiveness Program of NUST "MISiS" (No. K2-2017-006). NL gratefully acknowledges the Laboratory for Superconducting Metamaterials, NUST "MISiS" for its warm hospitality during visits.

-
- [1] R. C. McPhedran, I. V. Shadrivov, B. T. Kuhlmey, and Yu. S. Kivshar. Metamaterials and metaoptics. *NPG Asia Mater.*, 3:100–108, 2011.
- [2] N. I. Zheludev and Yu. S. Kivshar. From metamaterials to metadevices. *Nature Mater.*, 11:917–924, 2012.
- [3] R. El-Ganainy, K. G. Makris, M. Khajavikhan, Z. H. Musslimani, S. Rotter, and D. N. Christodoulides. Non-Hermitian physics and \mathcal{PT} symmetry. *Nature Phys.*, 14:11–19, 2018.
- [4] V. G. Veselago. The electrodynamics of substances with simultaneously negative values of epsilon and mu. *Usp. Fiz. Nauk*, 92:517526, 1967.
- [5] J. B. Pendry, A. J. Holden, W. J. Stewart, and I. Youngs. Extremely low frequency plasmons in metallic mesostructures. *Phys. Rev. Lett.*, 76:4773–4776, 1996.
- [6] J. B. Pendry, A. J. Holden, D. J. Robbins, and W. J. Stewart. Magnetism from conductors and enhanced nonlinear phenomena. *IEEE Trans. Microwave Theory Tech.*, 47:2075–2084, 1999.
- [7] D. R. Smith, W. J. Padilla, D. C. Vier, S. C. Nemat-Nasser, and S. Schultz. Composite medium with simultaneously negative permeability and permittivity. *Phys. Rev. Lett.*, 84 (18):4184–4187, 2000.
- [8] C. M. Bender and S. Boettcher. Real spectra in non-Hermitian Hamiltonians having \mathcal{PT} symmetry. *Phys. Rev. Lett.*, 80 (24):5243–5246, 1998.
- [9] C. M. Bender, D. C. Brody, and H. F. Jones. Complex extension of quantum mechanics. *Phys. Rev. Lett.*, 89:270401, 2002.
- [10] K. G. Makris, R. El-Ganainy, D. N. Christodoulides, and Z. H. Musslimani. Beam dynamics in \mathcal{PT} -symmetric optical lattices. *Phys. Rev. Lett.*, 100:103904, 2008.
- [11] Z. H. Musslimani, K. G. Makris, R. El-Ganainy, and D. N. Christodoulides. Optical solitons in \mathcal{PT} periodic potentials. *Phys. Rev. Lett.*, 100:030402, 2008.
- [12] J. Schindler, Z. Lin, J. M. Lee, H. Ramezani, F. M. Ellis, and T. Kottos. \mathcal{PT} -symmetric electronics. *J. Phys. A: Math. Gen.*, 45 (44):444029, 2012.
- [13] N. Lazarides and G. P. Tsironis. Gain-driven discrete breathers in \mathcal{PT} -symmetric nonlinear metamaterials. *Phys. Rev. Lett.*, 110:053901 (5pp), 2013.
- [14] S. R. White and L. J. Sham. Electronic properties of flat-band semiconductor heterostructures. *Phys. Rev. Lett.*, 47 (12):879–882, 1981.
- [15] D. S. Dessau, Z.-X. Shen, D. M. King, D. S. Marshall, L. W. Lombardo, P. H. Dickinson, A. G. Loeser, J. DiCarlo, C.-H. Park, A. Kapitulnik, and W. E. Spicer. Key features in the measured band structure of $Bi_2Sr_2CaCu_2O_{8+\delta}$: Flat bands at EF and Fermi surface nesting. *Phys. Rev. Lett.*, 71 (17):2781–2784, 1993.
- [16] E. H. Lieb. Two theorems on the Hubbard model. *Phys. Rev. Lett.*, 62 (10):1201–1204, 1989.
- [17] J. D. Bodyfelt, D. Leykam, C. Danieli, Xiaoquan Yu, and S. Flach. Flatbands under correlated perturbations. *Phys. Rev. Lett.*, 113:236403, 2014.
- [18] M. I. Molina. Flat bands and \mathcal{PT} -symmetry in quasi-one-dimensional lattices. *Phys. Rev. A*, 92 (6):063813, 2015.
- [19] Li Ge. Parity time symmetry in a flat band system. *Phys. Rev. A*, 92:052103, 2015.
- [20] N. Lazarides and G. P. Tsironis. SQUID metamaterials on a Lieb lattice: From flat-band to nonlinear localization. *Phys. Rev. B*, 96:054305, 2017.
- [21] D. Leykam, S. Flach, O. Bahat-Treidel, and A. S. Desyatnikov. Flat band states: Disorder and nonlinearity. *Phys. Rev. B*, 88:224203, 2013.
- [22] R. Khomeriki and S. Flach. Landau-Zener Bloch oscillations with perturbed flat bands. *Phys. Rev. Lett.*, 116:245301, 2016.
- [23] D. Leykam, A. Andreanov, and S. Flach. Artificial flat band systems: from lattice models to experiments. *Advances in Physics X*, 3 (1):1473052, 2018.
- [24] F. Perakis and G. P. Tsironis. Discrete nonlinear Schrödinger equation dynamics in complex networks. *Phys. Lett. A*, 375:676–679, 2011.
- [25] Bo Lu, Keiji Yada, M. Sato, and Y. Tanaka. Crossed surface flat bands of Weyl semimetal superconductors. *Phys. Rev. Lett.*, 114:096804, 2015.
- [26] Bo Liu, J. A. Baimova, S. V. Dmitriev, Xu Wang, Hongwei Zhu, and Kun Zhou. Discrete breathers in hydrogenated graphene. *J. Phys. D: Appl. Phys.*, 46:305302 (9pp), 2013.
- [27] Congjun Wu, D. Bergman, L. Balents, and S. Das Sarma. Flat bands and Wigner crystallization in the honeycomb optical lattice. *Phys. Rev. Lett.*, 99:070401, 2007.
- [28] Wang Yao, Shengyuan A. Yang, and Qian Niu. Edge states in graphene: From gapped flat-band to gapless chiral modes. *Phys. Rev. Lett.*, 102:096801, 2009.
- [29] Yi-Fei Wang, Zheng-Cheng Gu, Chang-De Gong, and D. N. Sheng. Fractional quantum Hall effect of hardcore bosons in topological flat bands. *Phys. Rev. Lett.*, 107:146803, 2011.
- [30] Yi-Fei Wang, Hong Yao, Zheng-Cheng Gu, Chang-De Gong, and D. N. Sheng. Non-abelian quantum Hall effect in topological flat bands. *Phys. Rev. Lett.*, 108:126805, 2012.
- [31] N. Y. Yao, C. R. Laumann, A. V. Gorshkov, S. D. Bennett, E. Demler and P. Zoller, and M. D. Lukin. Topological flat bands from dipolar spin systems. *Phys. Rev. Lett.*, 109:266804, 2012.
- [32] E. Tang, J.-W. Mei, and X.-G. Wen. High-temperature fractional quantum Hall states. *Phys. Rev. Lett.*, 106:236802, 2011.
- [33] Kai Sun, Zhengcheng Gu, Hosho Katsura, and S. Das Sarma. Nearly flatbands with nontrivial topology. *Phys. Rev. Lett.*, 106:236803, 2011.
- [34] T. Neupert, L. Santos, C. Chamon, and C. Mudry. Fractional quantum Hall states at zero magnetic field. *Phys. Rev. Lett.*, 106:236804, 2011.
- [35] S. Mukherjee, A. Spracklen, D. Choudhury, N. Goldman, P. Öhberg, E. Andersson, and R. R. Thomson. Observation of a localized flat-band state in a photonic Lieb lattice. *Phys. Rev. Lett.*, 114:245504, 2015.
- [36] R. A. Vicencio, C. Cantillano, L. Morales-Inostroza,

- B. Real, C. Mejía-Cortés, S. Weimann, A. Szameit, and M. I. Molina. Observation of localized states in Lieb photonic lattices. *Phys. Rev. Lett.*, 114:245503, 2015.
- [37] I. Sersić, M. Frimmer, E. Verhagen, and A. F. Koenderink. Electric and magnetic dipole coupling in near-infrared split-ring metamaterial arrays. *Phys. Rev. Lett.*, 103:213902, 2009.
- [38] N. N. Rosanov, N. V. Vysotina, A. N. Shatsev, I. V. Shadrivov, D. A. Powell, and Yu. S. Kivshar. Discrete dissipative localized modes in nonlinear magnetic metamaterials. *Opt. Express*, 19:26500, 2011.
- [39] L. Esaki. New phenomenon in narrow germanium $p - n$ junctions. *Phys. Rev. (Letters to the Editor)*, 109:603–605, 1958.
- [40] N. Lazarides, M. Eleftheriou, and G. P. Tsironis. Discrete breathers in nonlinear magnetic metamaterials. *Phys. Rev. Lett.*, 97:157406–4, 2006.
- [41] F. Tisseur and K. Meerbergen. The quadratic eigenvalue problem. *SIAM Rev.*, 43:235–286, 2001.
- [42] W. J. Duncan and A. R. Collar. Matrices applied to the motions of damped systems. *Phil. Mag.*, 19:197–219, 1935.
- [43] D. Afolabi. Linearization of the quadratic eigenvalue problem. *Computers & Structures*, 26 (6):1039–1040, 1987.
- [44] See Supplemental Material at [URL will be inserted by publisher] for more details on the classical augmentation procedure and the elimination of energy during time-integration.
- [45] S. Flach, D. Leykam, J. D. Bodyfelt, P. Matthies, and A. S. Desyatnikov. Detangling flat bands into Fano lattices. *Europhys. Lett.*, 105:30001, 2014.
- [46] S. Flach, D. Krimer, and Ch. Skokos. Universal spreading of wave packets in disordered nonlinear systems. *Phys. Rev. Lett.*, 102:024101 [4 pages], 2009.
- [47] P. Rosenau and J. M. Hyman. Compactons: Solitons with finite wavelength. *Phys. Rev. Lett.*, 70 (5):564–567, 1993.
- [48] M. Eleftheriou, B. Dey, and G. P. Tsironis. Compactlike breathers: Bridging the continuous with the anticontinuous limit. *Phys. Rev. E*, 62 (5):7540–7543, 2000.
- [49] F. Kh. Abdullaev, P. G. Kevrekidis, and M. Salerno. Compactons in nonlinear Schrödinger lattices with strong nonlinearity management. *Phys. Rev. Lett.*, 105:113901, 2010.

**SUPPLEMENTAL MATERIAL: FLAT BAND
ENGINEERING WITH \mathcal{PT} METAMATERIALS:
COMPACT LOCALIZED FLAT-BAND STATES**

*Dynamics of Electrically and Magnetically Coupled
 \mathcal{PT} Metamaterials*

The dynamic equations for the charge q_n in the capacitor of the n th split-ring resonator (SRR) of the binary \mathcal{PT} metamaterial with a balanced gain/loss configuration (Fig. 1), without nonlinearities or external driving flux, are

$$\frac{d^2}{d\tau^2} \{ \lambda'_M q_{2n} + q_{2n+1} + \lambda_M q_{2n+2} \} + \gamma \frac{d}{d\tau} q_{2n+1} + \{ \lambda'_E q_{2n} + q_{2n+1} + \lambda_E q_{2n+2} \} = 0, \quad (9)$$

$$\frac{d^2}{d\tau^2} \{ \lambda_M q_{2n-1} + q_{2n} + \lambda'_M q_{2n+1} \} - \gamma \frac{d}{d\tau} q_{2n} = + \{ \lambda_E q_{2n-1} + q_{2n} + \lambda'_E q_{2n+1} \} = 0, \quad (10)$$

where λ_E and λ_M are the electric and magnetic coupling coefficients between SRRs whose center-to-center distance is d (and correspondingly λ'_E and λ'_M are the electric and magnetic coupling coefficients between SRRs whose center-to-center distance is d' , with $d' < d$), γ is the gain/loss coefficient (defined as a positive real number, $\gamma > 0$), and τ is the normalized temporal variable in units of the inductive-capacitive (LC) frequency $\omega_{LC}^{-1} = \sqrt{LC}$ with L and C being the inductance and the capacitance of individual SRRs, respectively. In Eqs. (9) and (10), the subscript n takes the values $n = 0, 1, 2, \dots, (N/2) - 1$ and $n = 1, 2, 3, \dots, N/2$, respectively, with N being the total number of SRRs in the \mathcal{PT} metamaterial. Since the strength of both the electric and the magnetic interaction falls-off roughly as the inverse cube of the center-to-center distance between SRRs, and $d < d'$, the relations $\lambda_E > \lambda'_E$ and $\lambda_M > \lambda'_M$ should naturally hold. More details on the equivalent electrical circuit models, the derivation and normalization of Eqs. (9) and (10) can be found in Refs. [13] and [40] of the paper, and the references therein.

Eqs. (9) and (10) can be written in matrix form as

$$\hat{\mathbf{M}} \frac{d^2}{d\tau^2} \mathbf{Q} = \hat{\mathbf{K}} \mathbf{Q} + \hat{\mathbf{C}}_1 \frac{d}{d\tau} \mathbf{Q}, \quad (11)$$

where $\hat{\mathbf{M}}, \hat{\mathbf{C}}_1, \hat{\mathbf{K}}$ are $N \times N$ matrices, defined as

$$\hat{\mathbf{M}} = \begin{bmatrix} 1 & \lambda_M & 0 & 0 & 0 & 0 & 0 & \dots \\ \lambda_M & 1 & \lambda'_M & 0 & 0 & 0 & 0 & \dots \\ 0 & \lambda'_M & 1 & \lambda_M & 0 & 0 & 0 & \dots \\ 0 & 0 & \lambda_M & 1 & \lambda'_M & 0 & 0 & \dots \\ 0 & 0 & 0 & \lambda'_M & 1 & \lambda_M & 0 & \dots \\ 0 & 0 & 0 & 0 & \lambda_M & 1 & \lambda'_M & \dots \\ 0 & 0 & 0 & 0 & 0 & \lambda'_M & 1 & \dots \\ \vdots & \ddots \end{bmatrix}, \quad (12)$$

$$\hat{\mathbf{K}} = (-1) \begin{bmatrix} 1 & \lambda_E & 0 & 0 & 0 & 0 & 0 & \dots \\ \lambda_E & 1 & \lambda'_E & 0 & 0 & 0 & 0 & \dots \\ 0 & \lambda'_E & 1 & \lambda_E & 0 & 0 & 0 & \dots \\ 0 & 0 & \lambda_E & 1 & \lambda'_E & 0 & 0 & \dots \\ 0 & 0 & 0 & \lambda'_E & 1 & \lambda_E & 0 & \dots \\ 0 & 0 & 0 & 0 & \lambda_E & 1 & \lambda'_E & \dots \\ 0 & 0 & 0 & 0 & 0 & \lambda'_E & 1 & \dots \\ \vdots & \ddots \end{bmatrix}, \quad (13)$$

and

$$\hat{\mathbf{C}}_1 = -\gamma \begin{bmatrix} +1 & 0 & 0 & 0 & 0 & 0 & 0 & \dots \\ 0 & -1 & 0 & 0 & 0 & 0 & 0 & \dots \\ 0 & 0 & +1 & 0 & 0 & 0 & 0 & \dots \\ 0 & 0 & 0 & -1 & 0 & 0 & 0 & \dots \\ 0 & 0 & 0 & 0 & +1 & 0 & 0 & \dots \\ 0 & 0 & 0 & 0 & 0 & -1 & 0 & \dots \\ 0 & 0 & 0 & 0 & 0 & 0 & +1 & \dots \\ \vdots & \ddots \end{bmatrix}, \quad (14)$$

while $\mathbf{Q} = [q_1 \ q_2 \ q_3 \dots \ q_N]^T$ is an N -dimensional vector. Note that $\hat{\mathbf{M}}$ and $\hat{\mathbf{K}}$ in Eq. (12) are real tridiagonal symmetric matrices, while $\hat{\mathbf{C}}_1$ in Eq. (14) is a real diagonal matrix. We may define now an auxiliary N -dimensional array \mathbf{V} so that $\mathbf{V} = \frac{d}{d\tau} \mathbf{Q}$. Then, Eq. (11) is written as a system of $2N$ first order ordinary differential equations in time, as

$$\frac{d}{d\tau} \mathbf{Q} = \mathbf{V}, \quad (15)$$

$$\frac{d}{d\tau} \mathbf{V} = \hat{\mathbf{M}}^{-1} [\hat{\mathbf{K}} \mathbf{Q} + \hat{\mathbf{C}}_1 \mathbf{V}], \quad (16)$$

where $\hat{\mathbf{M}}^{-1}$ is the inverse of the matrix $\hat{\mathbf{M}}$. Eqs. (15) and (16) above are the ones which are integrated numerically in time.

Linear Dispersion Bands and Flat Band Engineering

Linear Dispersion.- By substituting into Eqs. (9) and (10) the trial solutions

$$q_{2n} = A \exp[i(2n\kappa - \Omega\tau)], \quad (17)$$

$$q_{2n+1} = B \exp[i((2n+1)\kappa - \Omega\tau)], \quad (18)$$

where κ is the normalized wavevector and Ω is the frequency in units of ω_{LC} , we obtain

$$[1 - \Omega^2 - i\gamma\Omega] A + [\phi e^{-i\kappa} + \phi' e^{+i\kappa}] B = 0, \quad (19)$$

$$[\phi' e^{-i\kappa} + \phi e^{+i\kappa}] A + [1 - \Omega^2 + i\gamma\Omega] B = 0, \quad (20)$$

where $\phi \equiv \lambda_E - \lambda_M \Omega^2$ and $\phi' \equiv \lambda'_E - \lambda'_M \Omega^2$. By requesting nontrivial solutions for the resulting stationary problem Eqs. (19) and (20), we obtain the frequency dispersion relation

$$\Omega_\kappa^2 \equiv \Omega_\kappa^2 = \frac{1}{2a} \left(-b \pm \sqrt{b^2 - 4ac} \right), \quad (21)$$

where

$$\begin{aligned} a &= 1 - (\lambda_M^2 + \lambda'_M)^2 - 2\lambda_M \lambda'_M \cos(2\kappa) \\ b &= 2(\lambda_E \lambda_M + \lambda'_E \lambda'_M) \\ &\quad + 2(\lambda_E \lambda'_M + \lambda'_E \lambda_M) \cos(2\kappa) - 2 + \gamma^2 \\ c &= 1 - (\lambda_E^2 + \lambda'_E)^2 - 2\lambda_E \lambda'_E \cos(2\kappa). \end{aligned} \quad (22)$$

For γ less than a critical value γ_c (i.e., $\gamma < \gamma_c$), the dispersion relation Eq. (21) results in a frequency spectrum with two bands separated by a gap. The value of γ_c depends on the other geometrical and physical parameters of the system, and separates the exact or unbroken \mathcal{PT} phase of the metamaterial ($\gamma < \gamma_c$) from the broken one ($\gamma > \gamma_c$).

Flat Band Condition.- A flat band (FB) is not ensured by the particular lattice type considered here, which is a simple one-dimensional lattice with two sites per unit cell. In order to obtain a FB in the frequency spectrum, the model parameters such as the coupling constants λ_E , λ'_E , λ_M , λ'_M and the gain/loss factor γ should be appropriately tailored. A condition that ensures the existence of a FB in the frequency spectrum of the \mathcal{PT} metamaterial should provide a relationship between the above-mentioned parameters. For obtaining such a condition, it is requested that

$$\frac{d(\Omega_\kappa^2)}{d\kappa} = 0 \Rightarrow \frac{d\Omega_\kappa}{d\kappa} = v_g = 0, \quad (23)$$

where v_g is the group velocity, for any κ 's in the first Brillouin zone. (Note that since both bands are optical, Ω_κ is non-zero for any κ and parameter values for which the \mathcal{PT} metamaterial is in the exact phase.) Then, from Eq. (23), we get after some calculations

$$b(ab' - ba')(ac' - ca') = a(ac' - ca')^2 + c(ab' - ba')^2, \quad (24)$$

where the a , b , and c have been defined in Eq. (22) and

$$a' \equiv \frac{da}{d\kappa} = +4\lambda_M \lambda'_M \sin(2\kappa),$$

$$b' \equiv \frac{db}{d\kappa} = -4(\lambda_E \lambda'_M + \lambda'_E \lambda_M) \sin(2\kappa), \quad (25)$$

$$c' \equiv \frac{dc}{d\kappa} = +4\lambda_E \lambda'_E \sin(2\kappa). \quad (26)$$

Eq. (24) can be simplified further to the following equation

$$b(ab' - ba')(ac' - ca') = a(ac' - ca')^2 + c(ab' - ba')^2. \quad (27)$$

By using a set of auxiliary parameters we rewrite a, b, c and a', b', c' as

$$\begin{aligned} a &= a_1 - a_2 \cos(2\kappa), & b &= b_1 + b_2 \cos(2\kappa), \\ & & c &= c_1 - c_2 \cos(2\kappa), \end{aligned} \quad (28)$$

$$\begin{aligned} a' &= +2a_2 \sin(2\kappa), & b' &= -2b_2 \sin(2\kappa), \\ & & c' &= +2c_2 \sin(2\kappa), \end{aligned} \quad (29)$$

where $a_1, a_2, b_1, b_2, c_1, c_2$ can be readily deduced by direct comparison of Eq. (28) with Eq. (22). By substitution of Eqs. (28) and (29) into Eq. (27) we get after tedious calculations a κ -independent equation

$$(a_1 c_2 - c_1 a_2)^2 + (a_1 b_2 + a_2 b_1)(b_1 c_2 + c_1 b_2). \quad (30)$$

Finally, by replacing $a_1, a_2, b_1, b_2, c_1, c_2$ in the earlier equation with their expressions in terms of $\lambda_E, \lambda'_E, \lambda_M, \lambda'_M$ and γ , and by factorizing the resulting expression (using Mathematica or otherwise), we get

$$\begin{aligned} &\left[\frac{1}{\mathcal{R}'} (1 - \lambda_M^2) + \mathcal{G} + \mathcal{R}' (1 - \lambda_E^2) \right] \\ &\times \left[\frac{1}{\mathcal{R}} (1 - \lambda_M^2) + \mathcal{G}' + \mathcal{R} (1 - \lambda_E^2) \right] = 0, \end{aligned} \quad (31)$$

where

$$\mathcal{R} = \frac{\lambda_M}{\lambda_E}, \quad \mathcal{R}' = \frac{\lambda'_M}{\lambda'_E}, \quad (32)$$

and

$$\mathcal{G} = -2 + \gamma^2 + 2\lambda_E \lambda_M, \quad \mathcal{G}' = -2 + \gamma^2 + 2\lambda'_E \lambda'_M. \quad (33)$$

Eq. (31) is the necessary and sufficient FB condition that we were looking for. In order to satisfy the condition Eq. (31), we have to find parameter sets $\{\mathcal{R}, \lambda'_E, \lambda'_M, \gamma\}$ or $\{\mathcal{R}', \lambda_E, \lambda_M, \gamma\}$ in four-dimensional parameter spaces which make the expression in either the first or the second squared brackets in Eq. (31) to be zero. These parameter sets, however, should also provide physically acceptable values for the coupling and gain/loss coefficients. For the geometrical configuration considered here, physically acceptable parameter values are those which zero the expression in the first squared brackets, i.e.,

$$\left[\frac{1}{\mathcal{R}'} (1 - \lambda_M^2) + \mathcal{G} + \mathcal{R}' (1 - \lambda_E^2) \right] = 0, \quad (34)$$

A parameter set $\{\mathcal{R}', \lambda_E, \lambda_M, \gamma\}$ which satisfy Eq. (34) completely flattens the upper frequency band while the lower one remains non-flat. The frequency spectrums for four (4) such parameter sets are shown in Fig. 7.

A Comment on the Coupling Coefficients.- The physically acceptable parameter values for λ_E , λ_M , and \mathcal{R}' used in the subfigures of Fig. 7 are around -0.12 , -0.40 and 0.93 , respectively. This choice is dictated by feasibility arguments: in order to tailor the coupling coefficients, several geometrical parameters related to the size and shape of the SRRs as well as their center-to-center distances should be adjusted. For the mutual orientation of the slits of the SRRs in the \mathcal{PT} metamaterial of Fig. 1, the coupling coefficients have been calculated accurately for a particular type of SRRs in Ref. [38] of our paper. According to that article (see their figure 1(a)), the coupling coefficients used in Fig. 7 as well as in Fig. 2(a) of our paper correspond to estimated distances $d \sim 2$ and $d' \sim 3.7$ in units of the SRRs' radii. Thus, it is in principle feasible to create a FB \mathcal{PT} metamaterial using SRRs of the type considered in Ref. [38] of our paper arranged in the configuration of Fig. 1 and d , d' as mentioned above.

The Quadratic Eigenvalue Problem

In order to eliminate the time-dependence form Eq. (11), we use the *ansatz*

$$\mathbf{Q} = \mathbf{Q}^e e^{i\Omega\tau}, \quad (35)$$

where \mathbf{Q} and \mathbf{Q}^e are N -dimensional vectors, so that $\frac{d}{d\tau}\mathbf{Q} = i\Omega\mathbf{Q}$, etc. By substitution of Eq. (35) into Eq. (11) we get

$$\{\Omega^2\hat{\mathbf{M}} + \Omega\hat{\mathbf{C}} + \hat{\mathbf{K}}\}\mathbf{Q}^e = \hat{\mathbf{0}}, \quad (36)$$

where $\hat{\mathbf{C}} \equiv i\hat{\mathbf{C}}_1$. Eq. (36) is a Quadratic Eigenvalue Problem (QEP), a special case of a Nonlinear Eigenvalue Problem. QEPs are customarily appear in the analysis of structures with physical damping; in such cases, nonlinear eigenvalue problem formulation is required to correctly describe the vibration of the system. Within this context, we replace in the following Ω with λ (the eigenvalue) and then obviously \mathbf{Q}^e is the eigenvector. The theoretical analysis and the numerical methods for QEPs usually proceed via linearization, i.e., via the embedding of the QEP (in general the nonlinear eigenvalue problem) into a larger linear eigenvalue problem. Using the classical augmentation procedure for the QEP Eq. (36), which transforms square matrices of order N to $2N$, we have the "generalized" (although linear) eigenvalue problem

$$\hat{\mathbf{A}}\mathbf{z} = \lambda\hat{\mathbf{B}}\mathbf{z}, \quad (37)$$

where $\hat{\mathbf{A}}$ and $\hat{\mathbf{B}}$ are the $2N \times 2N$ block matrices

$$\hat{\mathbf{A}} = \begin{bmatrix} \hat{\mathbf{0}} & \hat{\mathbf{M}} \\ -\hat{\mathbf{K}} & -\hat{\mathbf{C}} \end{bmatrix}, \quad \hat{\mathbf{B}} = \begin{bmatrix} \hat{\mathbf{M}} & \hat{\mathbf{0}} \\ \hat{\mathbf{0}} & \hat{\mathbf{M}} \end{bmatrix}. \quad (38)$$

It can be easily shown that Eq. (37) with the matrices $\hat{\mathbf{A}}$ and $\hat{\mathbf{B}}$ from Eq. (38) reduces to the QEP Eq. (36) for \mathbf{z} such that $\mathbf{z}^T = [\mathbf{Q}^{(e)} \ \lambda\mathbf{Q}^{(e)}]$. The usual way to solve the eigenvalue problem Eq. (37) is to multiply both sides of the equation with the inverse of $\hat{\mathbf{B}}$, $\hat{\mathbf{B}}^{-1} = \begin{bmatrix} \hat{\mathbf{M}}^{-1} & \hat{\mathbf{0}} \\ \hat{\mathbf{0}} & \hat{\mathbf{M}}^{-1} \end{bmatrix}$, so that

$$(\hat{\mathbf{B}}^{-1}\hat{\mathbf{A}})\mathbf{z} = \lambda\mathbf{z}, \quad (39)$$

with

$$(\hat{\mathbf{B}}^{-1}\hat{\mathbf{A}}) = \begin{bmatrix} \hat{\mathbf{0}} & \hat{\mathbf{I}} \\ -\hat{\mathbf{M}}^{-1}\hat{\mathbf{K}} & -\hat{\mathbf{M}}^{-1}\hat{\mathbf{C}} \end{bmatrix}, \quad (40)$$

where $\hat{\mathbf{I}}$ is the $N \times N$ identity matrix. The Standard Eigenvalue Problem (SEP) Eq. (39) can be solved with a standard eigenproblem solver for general complex matrices.

The solution of the SEP Eq. (39) provides all the eigenfrequencies (-values) Ω_κ and the eigenmodes \mathbf{Q}^e for the two frequency bands. Since the metamaterial is \mathcal{PT} symmetric (in the exact \mathcal{PT} phase, all the eigenvalues are real (their imaginary part is less than 10^{-15} for the parameter sets used in this work). In Fig. 8, the first four eigenmodes of the lower, non-flat band are shown. These modes are clearly extended and their imaginary part is generally very small. The four most localized eigenmodes of the upper, flat band are shown in Fig. 9, along with $|\mathbf{Q}^e|$ shown as red curves. These modes, as well as all the others that belong to the FB, correspond to the same eigenfrequency which in this case is $\Omega_{FB} \simeq 1.0378$.

Numerical Simulation

Eqs. (9) and (10), implemented with the boundary conditions $q_0(\tau) = 0$ and $q_{N+1}(\tau) = 0$, are integrated numerically with a standard fourth order Runge-Kutta algorithm with constant time-step. The time-step is typically $\Delta\tau = T_{FB}/nstep$, where $T_{FB} = 2\pi/\Omega_{FB}$, with $nstep = 500$ or 800 . (Larger time-steps can be also used without altering the results). The initial conditions are single-site excitations of the form $q_{n=N/2+1}(\tau=0) = A$, $q_n(\tau=0) = 0$ for $n \neq N/2+1$, and $\dot{q}_n(\tau=0) = 0$ for any n . For the figures in the paper, the amplitude of the initial state is typically taken to be $A = 0.1$, and the total number of SRRs in the \mathcal{PT} metamaterial is $N = 128$. Similar results can be obtained with smaller arrays as well. Also, compact two-site localized FB states may result from different type, sufficiently localized initial conditions. For $N_e = 16$ SRRs at each end of the metamaterial, gain has been replaced by equal amount of loss; these lossy parts remove the excessive energy provided by the initial condition towards the formation of a compact localized FB state. For parameter sets not satisfying the

flat band condition, Eq. (34), single-site initial conditions disperse rapidly in the lattice and no localization of any type is observed. This is illustrated in Fig. 10, in which the spatiotemporal evolution of a single-site excitation is shown for $\sim 2.5 \times 10^5$ time units. For obtaining these results, we have chosen a parameter set which provides a flat upper frequency band, i.e., $\mathcal{S} = \{\gamma = 0.01, \lambda_E = -0.1200046, \lambda_M = -0.0400493, \mathcal{R}' = 0.9291948\}$, and changed the value of \mathcal{R}' from 0.9291948 to 0.9. In Fig. 11, we follow the spatiotemporal evolution of an initially single-site excitation using a parameter set \mathcal{S}' whose parameter values are close to those in the set \mathcal{S} , i.e., $\mathcal{S}' = \{\gamma = 0.01, \lambda_E = -0.12, \lambda_M = -0.04, \mathcal{R}' = 0.93\}$. In this case, we actually observe the formation of a localized state, which however cannot reach a steady state. Instead, that state gradually becomes delocalized; for long enough times, the initial energy will spread over the whole \mathcal{PT} metamaterial (eventually all of the initial energy will be dissipated at its lossy ends).

Accelerating convergence to a steady flat-band state.- We should note that the relaxation of the energy of the \mathcal{PT} metamaterial in a steady, localized flat-band state is very slow, because of the \mathcal{PT} symmetry. In order to accelerate convergence to such a steady state and save

computational time, the energy which spreads out of the localization region is eliminated continually during half of the integration time, i.e., for $\tau_0/2$ time units, with τ_0 being the total integration time; this is how the results shown in Fig. 6(b) of the paper have been obtained. First, we split the total integration time τ_0 into two parts of equal size, $\tau_0/2$. During the first half, we set $q_n = \dot{q}_n = 0$ for $n = 1, \dots, N/2-3$ and $n = N/2+6, \dots, N$, every 10 periods $T_{FB} = 2\pi/\Omega_{FB}$ of integration. This does not affect the region in which we expect the compact localized FB state to form, i.e., the eight sites for $n = \frac{N}{2} - 2, \frac{N}{2} - 1, \dots, \frac{N}{2} + 4, \frac{N}{2} + 5$ (localization region). Note that for the chosen initial condition, the compact two-site FB state is generated at the sites $n = N/2 + 1$ and $n = N/2 + 2$, i.e., in the middle of the localization region. After the first half of integration (for times greater than $\tau_0/2$) we let the integration proceed without elimination of the energy for $\tau_0/2$ more time units. Using this procedure, the relaxation time towards the formation of a compact localized FB state is reduced by more than one order of magnitude. A comparison of the results obtained with and without energy elimination reveals that they are asymptotically identical in the localization region.

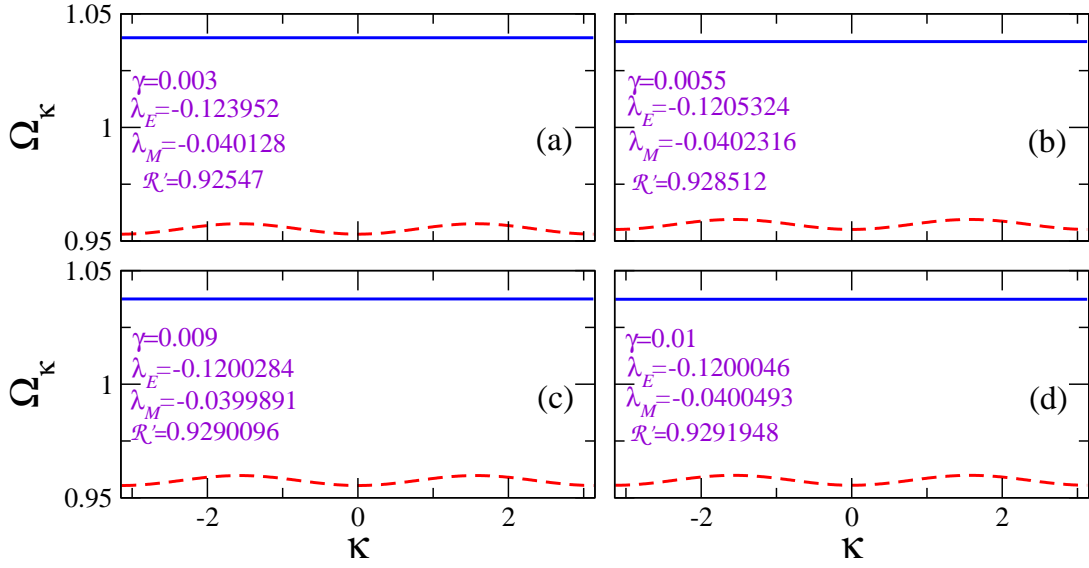


FIG. 7: (Color online) Frequency spectrums for a \mathcal{PT} metamaterial with balanced gain and loss for four different parameter sets satisfying Eq. (34). The values of these parameter sets are written on each subfigure. The upper band is completely flat in all cases.

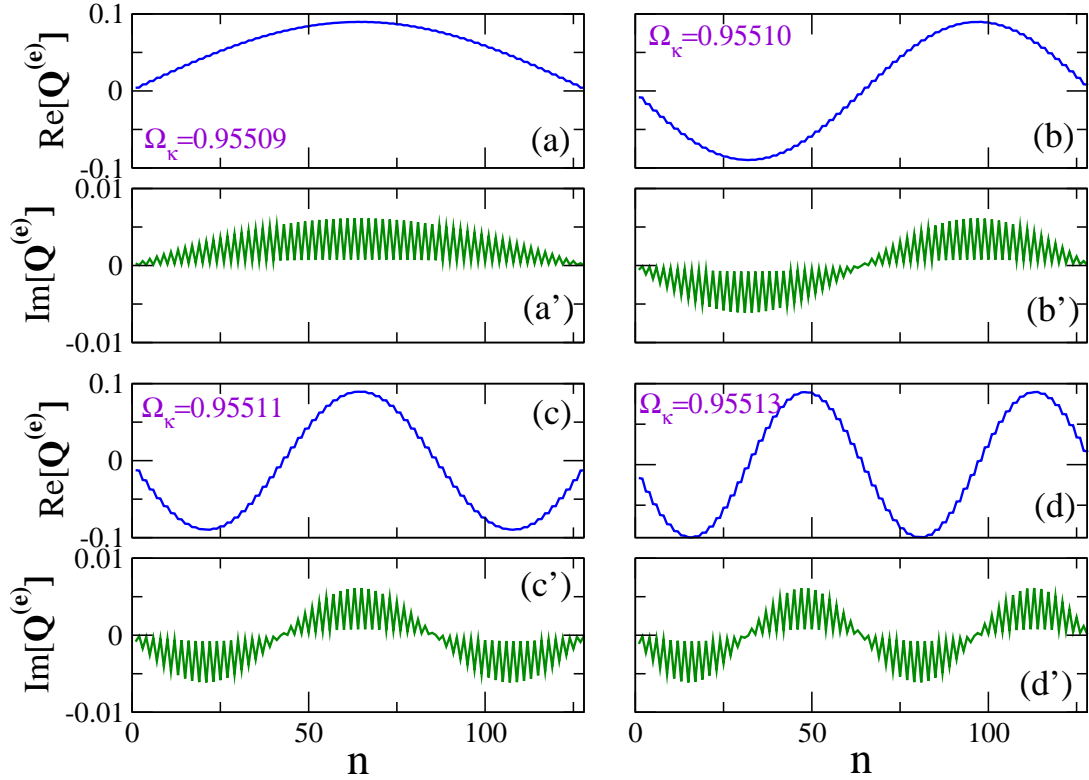


FIG. 8: (Color online) Real (blue) and imaginary (green) parts of the first four eigenmodes \mathbf{Q}^e that belong to the lower (non-flat) frequency band, obtained by solving the eigenvalue problem Eq. (39) for $N = 128$, $\gamma = 0.0055$, $\lambda_E = -0.1205324$, $\lambda_M = -0.0402316$, $\lambda'_E = -0.027$, and $\mathcal{R}' = 0.928512$. The corresponding eigenfrequencies are indicated on the figure.

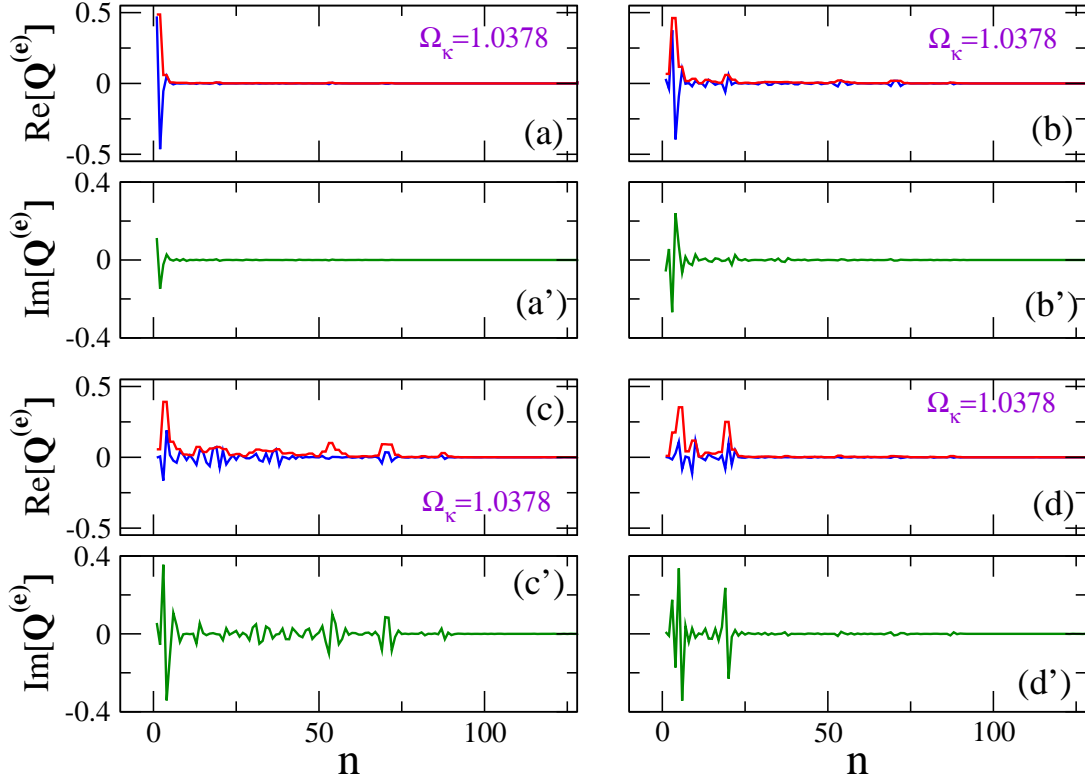


FIG. 9: (Color online) Real (blue) and imaginary (green) parts of the four most localized eigenmodes \mathbf{Q}^e that belong to the upper, flat frequency band, obtained by solving the eigenvalue problem Eq. (39). The corresponding eigenfrequencies are indicated on the figure. The parameters are as in Fig. 8. The red curves are the corresponding $|\mathbf{Q}^e|$ for each eigenmode.

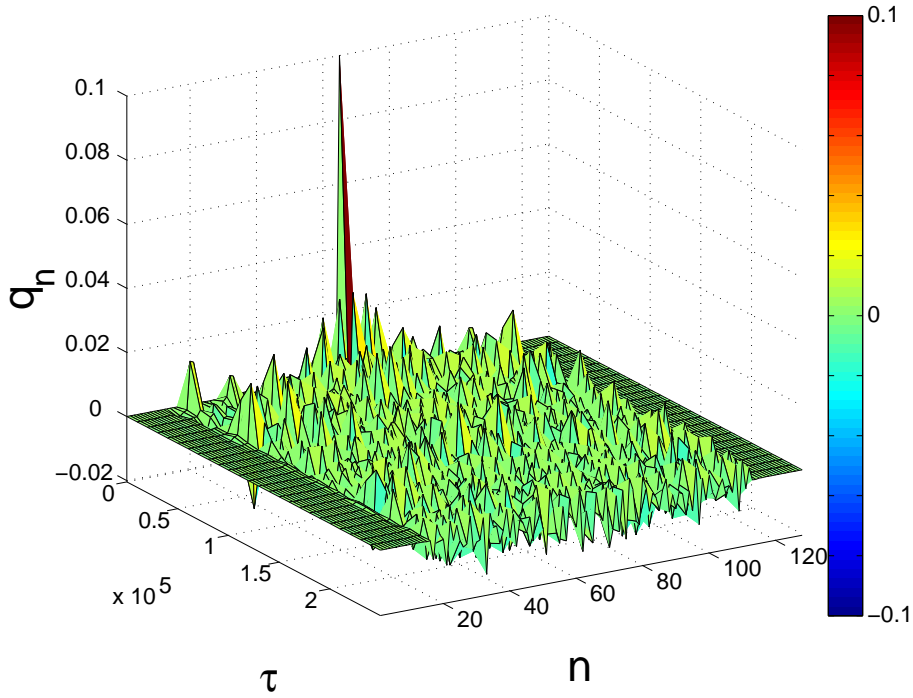


FIG. 10: (Color online) Spatiotemporal evolution of an initially single-site excitation of amplitude $A = 0.1$, for $N = 128$, $\gamma = 0.01$, $\lambda_E = -0.1200046$, $\lambda_M = -0.0400493$, $\lambda'_E = -0.027$, and $\mathcal{R}' = 0.9$. This parameter set does not provide a flat band (it would provide a flat band for $\mathcal{R}' = 0.9291948$, though), and thus the initial excitation disperses rapidly.

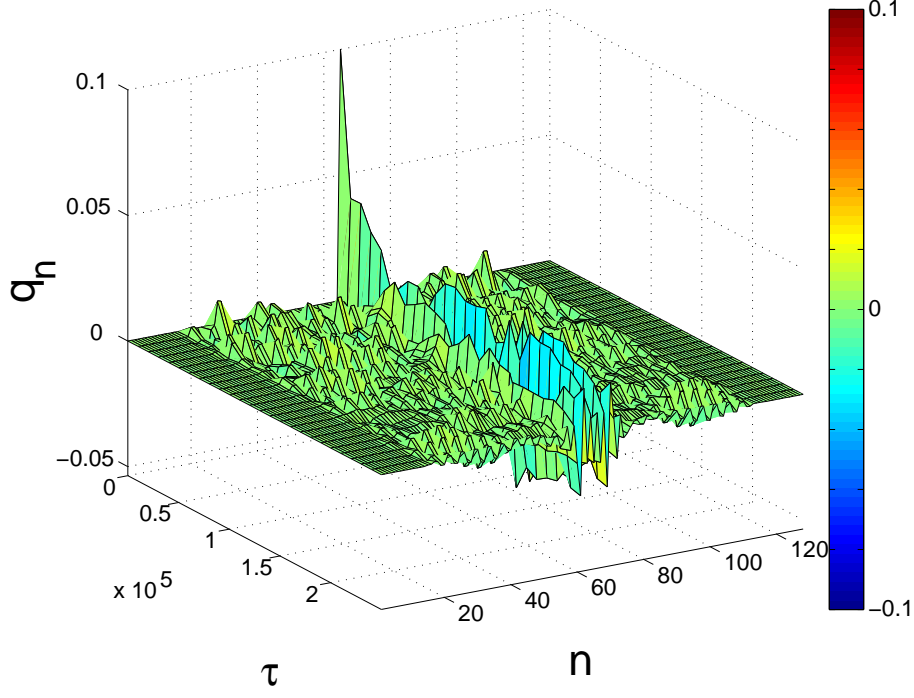


FIG. 11: (Color online) Spatiotemporal evolution of an initially single-site excitation of amplitude $A = 0.1$, for $N = 128$, $\gamma = 0.01$, $\lambda_E = -0.12$, $\lambda_M = -0.04$, $\lambda'_E = -0.027$, and $\mathcal{R}' = 0.93$. These values are close to the corresponding ones in the parameter set \mathcal{S} which provide a flat upper band. The initially single-site excitation gradually delocalizes.